Journal of Photochemistry and Photobiology A: Chemistry 216 (2010) 156–166

Contents lists available at ScienceDirect

Journal of Photochemistry and Photobiology A: Chemistry

journal homepage: www.elsevier.com/locate/jphotochem

The combinatorial atmospheric pressure chemical vapour deposition (cAPCVD) of a gradating substitutional/interstitial N-doped anatase TiO_2 thin-film; UVA and visible light photocatalytic activities

Andreas Kafizas, Colin Crick, Ivan P. Parkin*

Department of Chemistry, University College London, 20 Gordon Street, London WC1H 0AJ, UK

ARTICLE INFO

Article history:
Available online 6 July 2010

Keywords:
Nitrogen doping
Interstitial
Substitutional
Photocatalysis
Thin-film
Anatase

ABSTRACT

Combinatorial atmospheric pressure chemical vapour deposition (cAPCVD) was used to synthesise a film with gradating substitutional (N_s) and interstitial (N_i) nitrogen dopant concentrations across an anatase TiO_2 thin-film. A transition from predominantly N_s-doped, to N_s/N_i mixtures, to purely N_i-doped titania was observed by X-ray photoelectron spectroscopy (XPS) analysis of positions across the film. We believe this to be the first time that such a gradient from N_i to N_s-doping has been achieved by a CVD process in a single film. The film was characterized by X-ray diffraction, Raman, and atomic force microscopy. Film thicknesses and bandgap energies were calculated from Swanepoel and Tauc plot manipulations of transmittance spectra. The photocatalytic activity to UVA (365 nm = 1.75 mW cm^{-2}) light was assessed by monitoring colour changes in digital images of an even layer of intelligent ink deposited by an aerosol-spray method and by UV–visible spectroscopic assessment of the degradation of an aqueous methylene blue dye. The photo-activity to visible light (indoor white light source) was assessed by monitoring the degradation of a stearic acid over-layer. This allowed for the systematic investigation on the effect of N_s and/or N_i-doping in anatase TiO_2 and the dopant concentration on the thin-film's photocatalytic activity. The results indicated that N_s-doping of anatase titania causes detriment to the film's photocatalytic activity to UVA-light. It was also found that purely N_i-doped anatase made a marginally more active visible light photocatalyst than predominantly N_s-doping. The differences were related to increased recombination effects in N_s-doped systems versus N_i-doped systems. Films synthesized by the cAPCVD route analysed in conjunction with mapping analysis tools provide a shortcut to identifying numerous phases and compositions and their functional property relationships on a single film, offering a rapid method for analysis of phase-space.

© 2010 Elsevier B.V. All rights reserved.

1. Introduction

Anatase titanium dioxide (TiO_2) is the leading material for semiconductor photocatalyst applications due to its biological and chemical inertness, mechanical robustness durability to multiple photocatalytic cycles, relatively low cost and high photo-activity [1,2]. Anatase titania has been used for the degradation of organic pollutants, bacteria, cancer cells and viruses on nano-crystalline powders or thin-films [3–14]. The photo-degradation of the organic material occurs at the semiconductor's surface when photons greater than or equal to the bandgap energy is provided in the presence of oxygen. The bandgap energy of anatase titania (3.2 eV) requires photons that fall in the UVA portion of the electromagnetic spectrum or of higher energy (typically $\lambda \leq 388$ nm) to cause the photo-excitation of an electron from the valence to the conduction band and creation of an electron–hole pair. An energy stabilising migration of these holes (h^+) and electrons (e^-) predominantly formed within the bulk of the semiconductor to the surface of the film occurs. If recombination of the electron–hole pair does not occur, surface electrons reduce species such as atmospheric O_2 to superoxide O_2^-, which can be further reduced to H_2O and holes oxidise surface-bound hydroxyl groups into highly reactive hydroxyl radical species. The surface radicals/reduced species formed subsequently oxidise the surface-bound organic pollutant into mineral acids and CO_2.

A further consequence of photo-excitation of anatase titania is photo-induced superhydrophilicity (PSH), which has been shown to proceed by an alternative mechanism to photocatalysis, with the surface becoming more wettable due to hydroxyl formation. It is the combination of PSH and photocatalytic properties that have made anatase titania so highly suitable for self-cleaning thin-film coatings on glass [15] and tiles [16]; where the hydrophilic properties allow for greater surface-wetting and washing and the photocatalysis promotes degradation of organic residues. Although a range of

* Corresponding author. Tel.: +44 020 7679 4669; fax: +44 020 7679 7463.
E-mail address: i.p.parkin@ucl.ac.uk (I.P. Parkin).

1010-6030/$ – see front matter © 2010 Elsevier B.V. All rights reserved.
doi:10.1016/j.jphotochem.2010.06.034

products extending the use of anatase titania in water and air purification systems, sanitary-ware and deodorizing products have been commercially introduced [17], their use is limited to environments where sufficient UV-light is available for them to function. Although the more thermodynamically stable rutile form of titania [18] has a lower associated bandgap energy (3.0 eV); commercial applications of TiO_2 have predominantly featured the anatase phase. It has been a matter of considerable debate as to whether phase pure anatase, rutile or synergistic anatase–rutile mixtures provide a more effective photocatalyst [1]; however recent studies encompassing a range of pure/mixtures of anatase/rutile indicated phase pure anatase gave more photocatalytically active thin-films [19].

As a more significant portion of light is contained in the visible part of the solar spectrum, compared with UV-light, it has thus become an important goal to develop more red-shifted titania materials to enhance their photo-activity. As such, there have been a large number of studies aimed at modifying TiO_2 *via* doping or composite formation [20–27]. The inclusion of specific dopants alter the band structure of TiO_2 and can push the bandgap to more visible wavelengths; composites can also induce charge stability and transport of photo-excited electron–hole pairs within the material and increase the quantum efficiency.

Many research groups have found that N-doping of titania leads to greater visible light photo-activity [28–33]; however there is division on how this is achieved [2]. As the N dopant can enter the TiO_2 matrix by either direct substitution of an oxygen site (N_s) or by stationing itself interstitially (N_i) there is uncertainty in the literature as to which type of nitrogen insertion yields the more active visible light photocatalyst. Electron paramagnetic resonance (EPR) can be used to determine the nature of the N-dopant insertion in anatase titania powders [32,33]. X-ray photoelectron spectroscopy (XPS) has been shown to differentiate between N_i and N_s sites with N1s peaks at 400 eV and 396 eV respectively [34–36]. In contrast, some researchers suggest that oxygen vacancy (V_O) formation is fundamental to the visible light photocatalytic enhancement. In that scenario, the substitutional incorporation of nitrogen into anatase titania encourages V_O formation [37].

Theoretical DFT studies have modelled the effect on the density of states within anatase titania when N-doped with either N_s or N_i; with contrasting differences [38–40]. Calculations showed that N_s substitution causes the valence band to increase by 0.14 eV due to the overlap between nitrogen and oxygen 2p orbitals whereas N_i-doping creates an inter-band state 0.74 eV above the valence band [38,39]. The propensity to form oxygen vacancies in N-doped titania were shown to increase compared with an un-doped system. From calculations it was shown that the energy of V_O formation decreased from 4.2 eV in un-doped to 0.6 eV in N-doped anatase. In the case of N_s-doping, it is clear that the associated bandgap narrowing could induce a more active visible light photocatalyst in a single-electron excitation process. However, a dual-electron excitation process for N_i was suggested by Peng et al. [41]; with electrons initially photo-excited to the inter-band state and subsequently to the conduction band. Although it has been suggested that oxygen vacancies would encourage recombination, calculations by Zhao et al. indicated that V_O formation would create vacancies 1 eV below the conduction band and act as active traps that encourage photocatalysis [40]. Even though there is no consensus to the mechanism by which the visible light photocatalytic enhancement is achieved in N-doped TiO_2, there is agreement that a saturation point in N-doping occurs with a trade off between a narrowing of the bandgap and an increase in the detrimental effects of electron–hole recombination processes [29].

Chemical vapour deposition (CVD) is a technique that has been used to produce anatase titania thin-films of typically superior adhesion, durability and uniformity than the corresponding physical vapour deposition (PVD) counterpart [42–46]. However, single films with significant variations in thickness, phase and composition have been achieved using combinatorial atmospheric pressure chemical vapour deposition (cAPCVD) [47–52,19]. The investigation of such films, using high-throughput mapping analysis techniques [52–55], allowed for rapid determination of functional property relationships. For example, the effect of increased oxygen content within a vanadium oxynitride thin-film on the conductivity and reflectance properties [47]. However, cAPCVD was recently used to synthesise a N-doped thin-film with gradating N_s content and phase (anatase–rutile content) [48]. Photocatalytic activity mapping [53,54] of the film demonstrated the effect of N_s upon the films photo-activity to UVA 365 nm light in addition to the role of an increased rutile phase component. The nitrogen dopant was introduced into the TiO_2 matrix using ammonia gas as the source; analogous to previous work performed by Yates et al. [55]. In correlation with their APCVD produced N_s-doped thin-films, a decrease in the photocatalytic activity to UVA-light was also observed. APCVD deposited N_s-doped anatase TiO_2 thin-films were also produced by Duminica et al. using hydrazine as the nitrogen source. Films again showed lower photocatalytic activity to UVA-irradiation; however increased visible light activity was noted [56]. Contrastingly, using a t-butylamine nitrogen source, Dunnill et al. were able to synthesise purely N_i-doped anatase thin-films by APCVD [34–36]. Although these films were not tested to UVA-light, a marked increase in the visible light photocatalytic activity in the destruction of a stearic acid over-layer was observed.

From the literature, it is clear that the use of ammonia gas as a nitrogen source in APCVD synthesis encourages N_s-doping within anatase thin-films [48,49]; with higher ammonia concentrations encouraging the formation of a new phase, pseudo-brookite Ti_3O_4N, which is itself an active photocatalyst [50,51,19]. Although predominantly N_i insertion of anatase was observed when t-butylamine was used, it was suggested that the reaction proceeded through a thermal decomposition step to ammonia gas before surface-reaction and insertion [34–36]. It was therefore intuitive that a more heavily diluted concentration of ammonia gas during depositions may encourage N_i-doping.

In this paper we describe the combinatorial atmospheric pressure chemical vapour deposition (cAPCVD) synthesis of an anatase TiO_2 thin-film with gradating nitrogen dopant from predominantly N_s-doping to purely N_i-doping using a triple source of precursors: $TiCl_4$ [metal source], ethyl-acetate [oxygen source], and ammonia gas [nitrogen source]. The ammonia source was diluted with a plain flow of N_2 that enabled a significantly lower ammonia concentration during the deposition compared to a previous study [48]. This encouraged the formation of a N_s to N_i-doping gradient across the thin-film. Correlations of the effect of N_s and/or N_i-doping of anatase TiO_2 on the thin-film's physical properties and photocatalytic activities to UVA and visible light were assessed. This work also illustrates how the combinatorial APCVD approach can be used to rapidly analyse phase-space and how it can be used to identify optimum material properties.

2. Materials and methods

All chemicals used in this study were purchased from Sigma–Aldrich Chemical Co; resazurin 92%, hydroxyl ethyl cellulose (HEC) [average $M_v \approx 90{,}000$], glycerol 99.5%, isopropanol 99.98%, acetone 99%, ethyl-acetate 99%, and titanium (IV) chloride 99.9%. Nitrogen and ammonia (oxygen free) gas cylinders were supplied by BOC. The glass substrate, consisting of a standard piece of 3.2 mm thick float glass coated with a 50 nm SiO_2 barrier layer that inhibited ion diffusion from the glass, was supplied by the Pilkington NSG Group.

Table 1
Displaying the deposition parameters used in the cAPCVD synthesis of an anatase TiO_2 thin-film with gradating N-dopant from predominantly substitutionally doped (N_s) to purely interstitially doped (N_i) and varying dopant concentrations.

Temperature (°C)					Flow *v* rate (L min^{-1})					Deposition time (s)
Reactor	Mixing chambers		Bubblers		N_2		NH_3	N_2		
	A	B	$TiCl_4$	$CH_2OC(O)CH_3$	A	B		$TiCl_4$	$CH_2OC(O)CH_3$	
500	226	245	45	43	2.0	1.0	0.02	2.0	0.8	40

2.1. Film synthesis

A single phase anatase TiO_2 thin-film with gradating levels of nitrogen insertion from predominantly substitutional (N_s) to purely interstitial (N_i) doping was synthesised by a cAPCVD technique. A cold-walled reactor was used with the film deposited onto a standard float glass slide of dimensions 50 mm × 225 mm × 3.2 mm (horizontal × lateral × thickness). The film was deposited on the top-surface of the glass slide that contained a barrier layer of SiO_2 (≈50 nm thick). This prevented ions within the glass (i.e. Na, Mg, Ca) to migrate into the synthesised thin-film. The substrate was pre-washed with acetone, isopropanol, and air-dried prior to use. The combinatorial atmospheric pressure chemical vapour deposition (cAPCVD) apparatus used to deposit the film was previously reported [53].

$TiCl_4$ [Bubbler 1] and ethyl–acetate [Bubbler 2] were volatized in heated bubblers. The reagents were transported to mixing chamber A by a N_2 carrier gas and combined with a plain line of N_2. Ammonia gas was transported under its own vapour pressure to mixing chamber B and then combined with a plain line of N_2, producing a more diluted N source. The reagents passed through their respective mixing chambers and then passed a double-entry baffle manifold, which inhibited their mixing until inside the reactor. This produced the conditions for the combinatorial aspect of this work, as the oxygen (ethyl-acetate) and nitrogen (ammonia) sources entered from opposite sides of the reactor. This created a horizontal gradient in the O:N ratio present in the precursor mix and thus a range of deposition conditions. The parameters used to achieve the combinatorial film in this study are displayed in Table 1.

2.2. Analytical methods

All positions characterised by various techniques are specified in Fig. 1, which shows the grid reference systems used throughout the paper on top of an underlying digital image of the combinatorial thin-film for 528 uniquely identified positions.

X-ray diffraction (XRD) mapping of 90 positions (Table 2) was performed on a micro-focus Bruker GADDS powder X-ray diffractometer with a monochromated Cu $K_{\alpha 1}$ (1.5406 Å) source, CCD area X-ray detector capable of 0.01° resolution in 2θ and an automated X–Y moveable stage. The instrument was used in the glancing incident angle geometry that is best suited for the investigation of films (θ_1 = 5°). Raman spectroscopy mapping was performed on a Renishaw 1000 spectrometer using a 632.8 nm laser, calibrated to the emission lines of graphite at 2 mW. The 90 positions analysed (Table 2), manoeuvred using an X–Y stage, were analysed over the 100–800 cm^{-1} range. Atomic force microscopy (AFM) was conducted on a Veeco Dimension 3100 in air using a contact operating mode and a silicon tipped cantilever over sample areas of 1 μm × 1 μm over 15 grid positions across the film (Table 2). Transmittance spectra were recorded over the 300–2500 nm range on a Helios double beam instrument. Film thicknesses were evaluated using the Swanepoel method [57] from interference fringes and band-gaps were derived from Tauc plot extrapolations [58]. By approximating linear growth between fringes, the thickness at the refringence boundaries and the 528 grid positions between/on the boundaries were determined. X-ray photoelectron spectroscopy (XPS) was performed at Cardiff University using a Kratos Axis Ultra-DLD photoelectron spectrometer using monochromatic Al-K_α radiation for 5 positions across the film (Table 2). Survey and high resolution scans were preformed before argon ion sputtering (30 s) the surface for a total of 5 cycles to attain a compositional depth profile. Survey scans were collected in the range 0–1100 eV (binding energy) at a pass energy of 160 eV. Higher resolution scans were recorded for the principal peaks of Ti (2p), O (1s), N (1s), C (1s) and Si (2p) at a pass energy of 40 eV. The peaks were modelled using the CasaXPS software system to determine their area and peak positions [59]. Peak positions were adjusted to adventitious carbon and peak areas were adjusted using sensitivity factors [60] to determine film composition.

Table 2
Grid positions analysed by each characterisation method employed.

Characterisation methods	Positions analysed
X-ray diffraction, Raman	Columns B, D, F, H, J, L; numbers 1, 4, 7, . . ., 37
Transmittance	
Swanepoel thickness	Between interference contours (Fig. 5(b))
Tauc band gap	J3, D12, J33, D39
Atomic force microscopy	Columns B, F, J; numbers 1, 10, 19, 28, 37
X-ray photoelectron spectroscopy	J3, D12, J33, D39
Photocatalytic activity	
UVA-light	
Intelligent ink	All 528 positions
Ethylene blue	J3, D12, J33, D39
White light	
Stearic acid	J3, D12, J33, D39

2.3. Photocatalysis methods

2.3.1. Intelligent ink (UVA-light)

The combinatorial film was washed in distilled water, rinsed with isopropanol and irradiated for 1 h with UVC 254 nm light (Vilber Lourmat 2 × 8W VL-208G-BDH/VWR Ltd.) to clean and activate the surface. Intelligent ink, formulated as prepared by Mills et al. [61], was loaded into an aerosol-spray gun (SIP Emerald Spray Gun/Halfords Plc.) The ink comprised of 3 g of a 1.5 wt% aqueous solution of hydroxyl ethyl cellulose (HEC) polymer, 0.3 g of glycerol and 4 mg of the redox dye, Resazurin (Rz). The film was walled mounted and spray-coated (air pressure feed = 3.5 bar) with an even layer of the ink. The photocatalytic reduction reaction was monitored by a digital photographic method between UVA 365 nm light (Vilber Lourmat 2 × 8W VL-208BL-BDH/VWR Ltd, 230 V/50 Hz–spectral output displayed in supplementary information 1a) irradiations [53,54]. Digital TIF images (200 ppi) were recorded using an Epson Perfection 1200 Photo Scanner and Windows Scanner Software. Red-green-blue values from digital images were acquired using custom-made software, entitled RGB Extractor©, written using Visual Basic 6.0 and available for free download [62]. Red-green-blue values were averages of 100 colour data pixels (10 × 10 squares) centred on the desired positions. The software could automatically assign the 528 locations designated

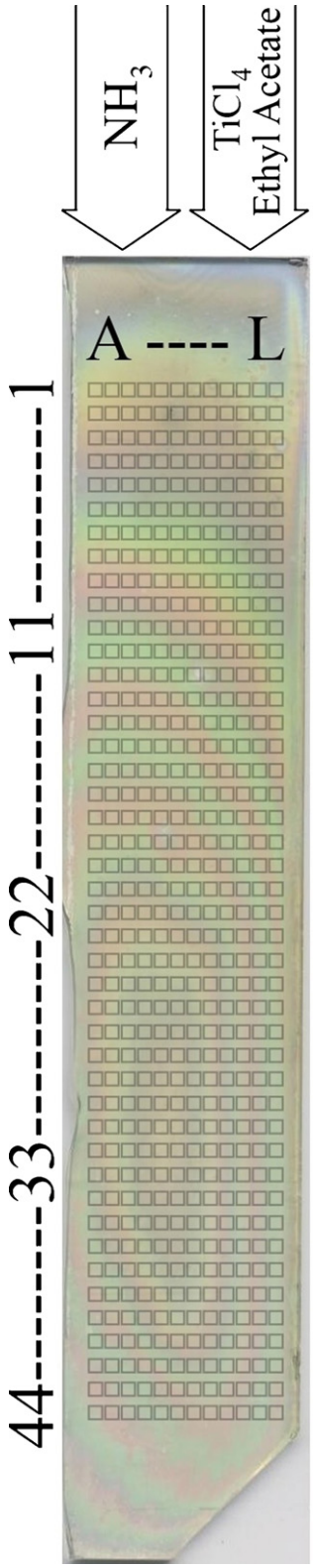

Fig. 1. Diagram and table representing the grid reference system and positions analysed for 528 uniquely identified positions. The grid-map is superimposed over an image of the combinatorial film; with gradating N content and type of insertion from predominantly N_s to purely N_i-doping within an anatase TiO_2 phase produced by cAPCVD. The alteration in colour was due to interference caused by varying thickness across the film. This was desired as it allowed the effect of thickness on the photocatalytic activity to also be studied. The positions of the gas inlets and where each reagent entered the reactor with respect to the film are also shown; with row 1 lying closest to the reactor inlet and row 44 lying closest to the exhaust. Grid positions were 4 mm apart in rows and 2 mm apart in columns.

to be colour extracted and systematically extract the red-green-blue averages instantaneously over all positions for each up-loaded image.

2.3.2. Methylene blue solution (UVA-light)

The photocatalytic degradation of methylene blue (MB) analysed by UV–visible spectroscopy over the 400–800 nm range on a PerkinElmer Lambda 25 UV/VIS spectrometer for four sample off-cuts from the combinatorial film centred at designated positions (Table 2) in addition to a titania standard. Samples were affixed to a custom-made measurement cell that consisted of a plastic cuvette transparent on three sides and holed on the fourth. The hole, centred on the test position, was 25 mm high and 8 mm wide; exposing a 2 cm^2 area to the MB solution. Approximately 15 surrounding grid positions were exposed in total; therefore an average rate centred on the designated position was derived.

An aluminium frame held the sample and the cuvette together with a silicon seal providing a water tight boundary. A stirrer bead was used to ensure uniform dispersion and aeration of the system. This resulted in a reservoir of MB solution in contact with the photocatalyst surface. The concentration of MB solution was made up such that the maximum absorbance (≈650 nm) was approximately 1 absorption unit. Any surface-dye absorption was first allowed to reach equilibrium in the dark for 1 h before beginning the photocatalysis reaction, where a 1–2% drop in the absorbance was observed. The destruction of MB was then followed as a function of time by the change in height of this absorbance maximum in 30 min intervals for a total of 6 h; with max absorbance decreases ranging from 5 to 20% over the period.

2.3.3. Stearic acid (visible white light source)

The photocatalytic mineralisation of stearic acid was tested against the same four sample off-cuts from the combinatorial film (Table 2), titania standard and a blank. Samples were affixed to measurement cells centred on the test position; exposing a 1 cm^2 area. Approximately 5 surrounding grid positions were exposed in total; therefore an average rate centred on the designated position was derived. The films were washed with propan-2-ol and photocleaned for 1 h using UVC 254 nm irradiation. Samples were coated with a waxy stearic acid over-layer (0.02 M solution in methanol) by depositing a few solution droplets onto the films surface. After spinning the samples at 1000 rpm for 10 s, the samples were oven dried for 1 h at 50 °C to ensure the complete evaporation of methanol. The samples were then irradiated under a white light source (GE lighting 2D fluorescent GR10q- 835 white, 28W [15,000 lux]–spectral output in supplementary information 1b) masked with a UV filter (Optivex™). The decrease in absorbance of C–H symmetric/anti-symmetric stretches in the 2980–2800 cm^{-1} infra-red range due to photocatalytic oxidation was monitored by Fourier transform infrared (FTIR) spectroscopy using a Perkin Elmer RX-I instrument. The change in peak area can be related to the concentration of stearic acid on the film's surface and converted into a photocatalytic degradation rate (molecules degraded cm^{-2} s^{-1}) [61].

3. Results and discussion

3.1. Physical characterisation

A combinatorial anatase thin-film with gradating N dopant from predominantly substitutional insertion (N_s) to purely interstitial insertion (N_i) was achieved by a cAPCVD technique. The film was grown at a substrate temperature of 500 °C by reaction of $NH_{3(g)}$, $TiCl_{4(g)}$ and ethyl $acetate_{(g)}$. Interference fringes, characteristic of thin-films with high refractive indices were observed (Fig. 1). This demonstrated the variation in thickness across and along the film, with the contours indicating that the middle-bottom section of the

Table 3
Substitutional (N_s) and interstitial (N_i) N-doping (at %) of 5 analysed grid positions across a combinatorial anatase thin-film made by a cAPCVD synthesis. Values are averages of the bulk from XPS depth profile analysis.

	N_s-doping/N_i-doping (at.%)			
	D	G	J	
3			11.0/2.2	3
12	5.8/1.3			12
19		5.7/1.0		19
33			0.0/4.3	33
39	9.3/2.6			39
	D	G	J	

film was thickest. During deposition, the centre of the underlying carbon heating block was slightly hotter (515 °C) than the edge of block (485 °C), thereby encouraging more rapid film growth in the middle section of the film and indicative of a surface-reaction rate limited growth mechanism [48]. From thicknesses derived by the Swanepoel method and contour extrapolations [48] of the 528 grid positions, the median growth rate across the film was 11.7 nm/s (standard deviation 4.5 nm/s) at a substrate temperature of 500 °C. The film also displayed a yellowish tint, characteristic of N_s-doping in titania samples [48]. Visual inspection showed the yellowish tint to be greatest in the top section of the film (Fig. 1—Row 1), decreasing outwards in a diagonal fashion, to a more transparent looking film in the bottom-right; thus demonstrating the desired gradating nature of N-dopant concentration across the film. A deeper yellow-tint was attributed to a greater concentration of N-doping. It was therefore intuitive (and later confirmed by XPS analysis, Table 3) that the greatest concentration of N was observed nearest to where the N-source entry position was located (Fig. 1). Films were adhesive and impervious to 24 h immersion in common solvents such as water, acetone and isopropanol. The films all passed the Scotch® tape test and were impervious to scratching with a stainless steel stylus. However, the film and glass substrate could be scratched with a diamond tip.

3.2. Characterisation

3.2.1. X-ray photoelectron spectroscopy

The oxidation state and environment of constituent elements were investigated by X-ray photoelectron spectroscopy (XPS) depth profile analysis of 5 positions distributed across the film (Table 3). Peak positions were calibrated relative to an adventitious trace surface carbon impurity taken to be at a binding energy of 284.5 eV [60]. Depth profiling confirmed the presence of only titanium, oxygen and nitrogen in the bulk. Peak deconvolution analysis within the N 1s range (390–420 eV) yielded three distinct surface environments across the film. Example spectra of the most N_s-doped (J3—Fig. 2a) and N_i-doped (J33—Fig. 2b) positions, including depth profiles, are shown in Fig. 2.

Peaks at 407.0 eV is related to the presence of surface-bound nitrogen in a high oxidation state (N^{5+}); most plausibly a nitrate species that formed on the film's surface upon cool down of the film inside of the reactor [47]. For position J3, the peak seen at 395.6 eV related to a highly reduced nitrogen species (N^{3-}). As no separate cubic TiN phase was observed in XRD patterns or Raman spectra (*vide infra*) the peak was attributed to a direct substitution of an oxygen site within the tetragonal anatase TiO_2 lattice (N_s-doping). The last of peaks observed at 399.7 eV related to either the presence of surface-bound nitrogen γ-N_2 (N^0) or interstitially doped N_i (N^0) [48]. The presence of surface-bound nitrogen species is common in APCVD synthesised thin-films deposited using a N_2 carrier gas so depth profiling was used to distinguish between nitrogen bound to the surface and nitrogen trapped within the bulk. This unveiled the presence of significant levels of interstitial nitrogen doping (N_i)

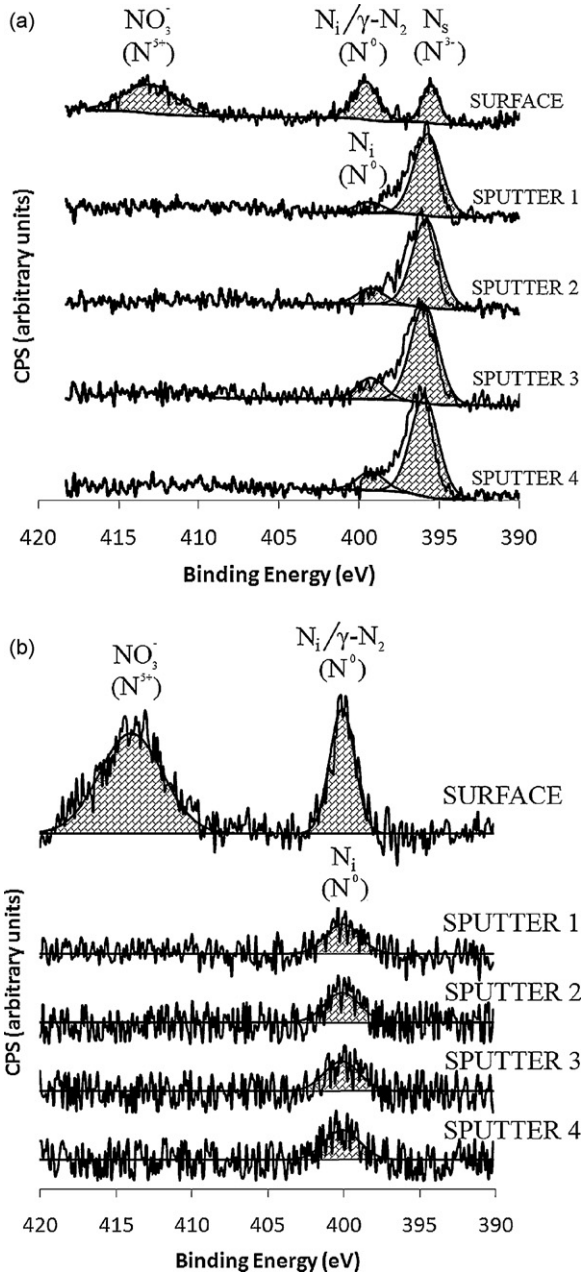

Fig. 2. XPS spectra of the surface and subsequent depth profiling within the N1s energy range (390–420 eV) at positions (a) J3 and (b) J33. After sputtering the sample with Ar ions for 30 s the surface nitrates and γ-N_2 were removed, showing the bulk N_i/N_s-dopant that remained within the bulk. Subsequent surface sputtering (2–4) showed the consistency of the N-dopant concentration throughout the material.

at all positions analysed within the bulk (Table 3). Depth-profiling also showed substitutional doping (N_s) to be present within the core of all positions as well, except at position J33, where solely interstitial doping occurred (Fig. 2b). Gaussian modelling of peak areas allowed the doping concentration to be determined relative to titanium (2p). N_s and N_i-doping levels for the 5 grid positions analysed are shown in Table 3.

Position J3 showed the highest levels of N_s-doping (11.0 at %) and position J33 showed the lowest, with no N_s-doping detected. In contrast, the highest level of N_i-doping was observed at J33 (4.3 at.%). Position J33 lay furthest from the gas inlet, where the nitrogen source (NH_3) flowed into the reactor during the deposition. Assuming this position experienced a lower overall ammonia concentration during the reaction, N_i-doping over N_s-doping may

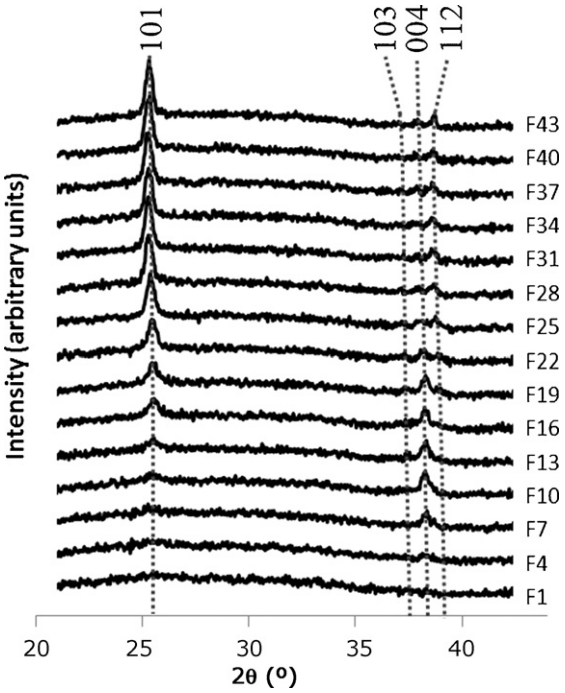

Fig. 3. Stacked (a) XRD patterns and (b) Raman spectra of the 15 positions analysed along Column F; an anatase titanium dioxide thin-film with gradating N-doping from predominantly N_s to purely N_i insertion synthesised by a cAPCVD method.

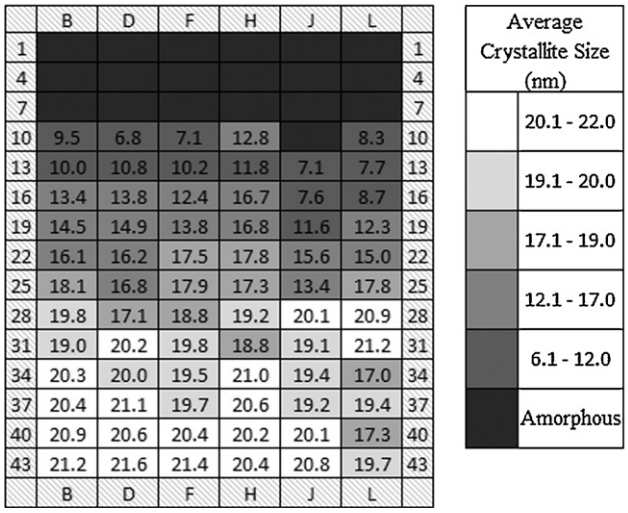

Fig. 4. Colour coded map representation of the average crystallite size (nm) derived from the Scherrer equation [64]. A transition from an amorphous film in the early rows to an increasingly crystalline thin-film in the latter rows was observed. Greatest film crystallinity was seen in the bottom left section of the film, decreasing outwardly in a diagonal fashion.

be encouraged by lower local ammonia concentrations. From the positions analysed, wide ranging levels of N-doping from $0.0 \leq N_s$-doping (at.%) ≤ 11.0 to $1.0 \leq N_i$-doping (at.%) ≤ 4.3 were present. The level of N_i-incorporation seen in this film was significantly greater than what has normally been seen; where levels up to only ≈0.5 at % were achieved [34–36].

3.2.2. X-ray diffraction

All diffraction patterns analysed across the combinatorial film featured solely the anatase TiO_2 ($I4_1/amdz$, $a = 3.782$ Å, $c = 9.504$ Å) phase. Corresponding Raman spectra confirmed the presence of this single phase. Fig. 3 displays some example stacked XRD patterns and for positions analysed along Column F.

A large variation in film crystallinity was observed. Low peak intensities in XRD patterns were observed at positions in the early rows, which lay closest to the gas inlets during the deposition. More intense peaks were seen in the latter rows that lay closer to the exhaust. A gradual increase in film crystallinity was observed upon movement from the early to latter rows, as seen in Column F in Fig. 3. The Scherrer equation [64] was applied to the most prominent diffraction peak observed in XRD patterns (25.4°, 1 0 1 plane). This determined the average crystallite size across the film and a colour coded schematic of the results are shown in Fig. 4. As rows 1, 4, 7 and 10 were predominantly amorphous, the average crystallite size could not be determined (Fig. 4). The transition from typically amorphous film growth in the early rows to an increasingly crystalline film growth in the latter rows was quantified. The crystallinity of the film seemingly held no bearing on the level of N-insertion achieved, as approximately equivalent total levels of N-doping at J3 (13.2 at.%,) and J39 (11.9 at.%) were determined by XPS.

An alteration in the relative heights of XRD plane intensities was also seen, due to preferences in the orientation of film growth. For example, a transition from preferred growth in the 004 plane (positions F7–F19) to preferred growth in the 101 plane (positions F22–F43) was seen along Column F (Fig. 3). These variations, typical for films made by cAPCVD [19], added to the combinatorial nature desired for the experiment. The degree of preferred orientation in the 1 0 1 plane was calculated by dividing the 1 0 1 peak area by total peak areas. The greatest preference of film growth in the 1 0 1 plane was seen in the bottom-left section of the film, which decreased outwardly in a diagonal fashion toward the top-right section. The observed trend in the degree of preferred orientation was very similar to that of crystallinity; where increasing crystallite size went in hand with a greater degree of preferred orientation in the 101 plane and a linear correlation coefficient of $r^2 = 0.76$ was observed. The pattern did not seemingly correlate with underlying film thickness by observation of changes in the interference patterns seen by eye. These interference contours peaked seemingly in the central section of the early row 30s whereas preferred orientation peaked at B40.

3.2.3. Atomic force microscopy

Atomic force microscopy was conducted on 15 positions across the combinatorial thin-film.

Collectively, smooth surface topographies were observed, typical for CVD produced thin-films. Nonetheless, slight discrepancies in the surface roughnesses were observed between samples. Deflection images of the 5 positions analysed along Column F are shown in Fig. 5a. The marginal increase in the coarseness of the surface seen by eye was quantified by root mean squared surface roughness derivations (Rq). These roughness values were plotted in a 3D-bar chart against underlying grid position (Fig. 5b). An increasing surface roughness correlated with increasing distance from the precursor gas-inlet added to the combinatorial nature of the film.

3.2.4. Swanepoel analysis

The transmittance spectra at designated positions between contour boundaries on the combinatorial N-doped anatase TiO_2 film were measured in the 300–2500 nm range (Fig. 6a). An increase in the wavy nature of spectra from early to latter rows occurred; indicative of increasing film thickness. With knowledge of the dependence of the material's refractive index with wavelength, the interference maxima and minima can be used to accurately (<1% error) determine film thickness using the Swanepoel method [57]. After determining the thickness between select contours, the thickness at the refringence boundary and the 528 grid positions

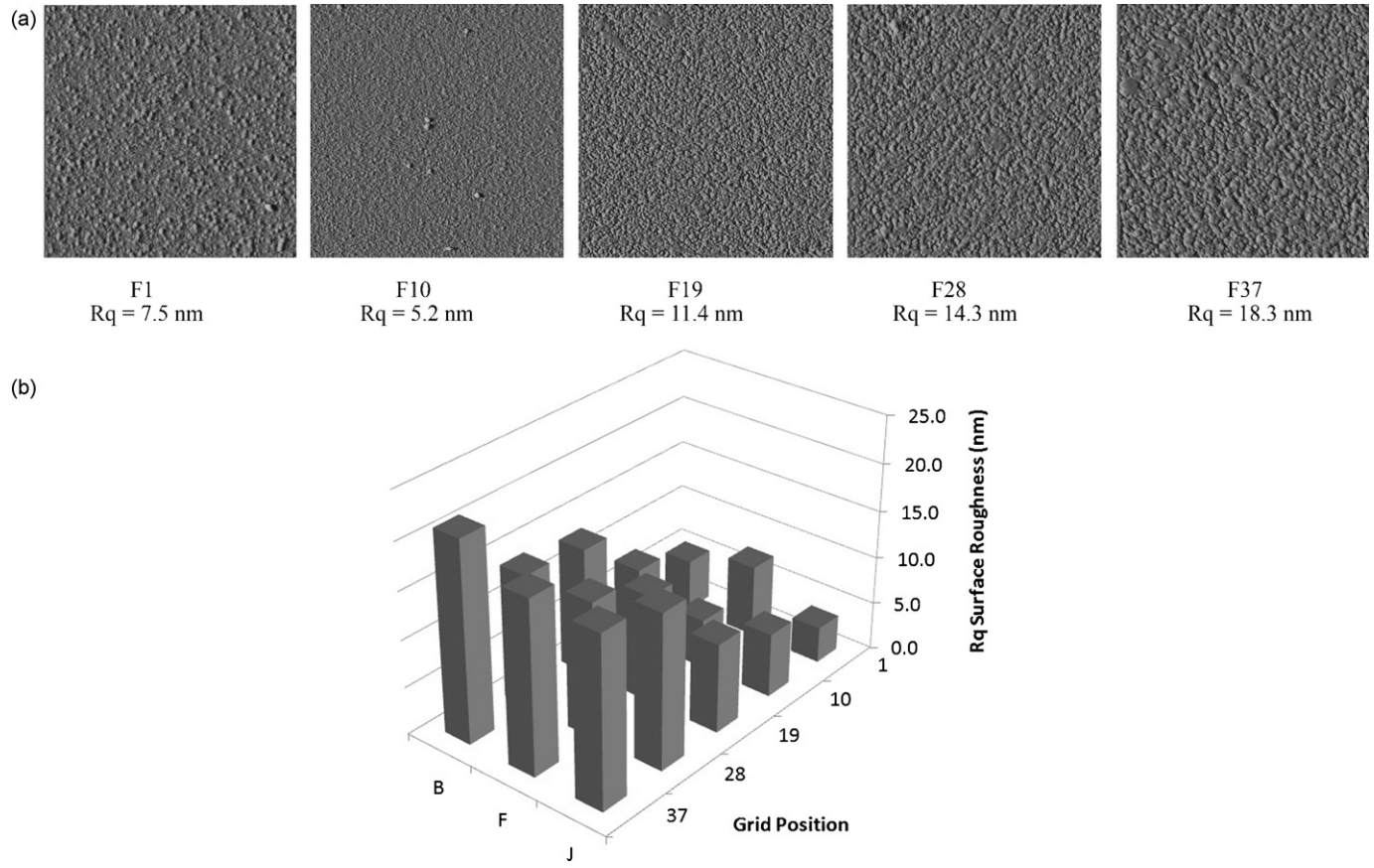

Fig. 5. (a) Example AFM images of the positions analysed along Column F; a combinatorial anatase thin-film synthesised by cAPCVD at 500 °C with gradating levels of N-doping from predominantly N_s to purely N_i insertion. (b) A 3D bar plot of the surface roughnesses taken from all grid-positions analysed across the film demonstrating the general increase in the surface roughness with increased distance from the precursor gas-inlets.

between and at the boundaries were calculated by approximating linear growth between fringes [48]. A colour coded map of film thickness versus grid position quantified the variation in thickness seen by eye (Fig. 6b).

3.2.5. Reaction chemistry

Knowledge of the precursor temperatures and carrier gas flow rates allowed molar flow rates to be determined (Table 4) [65]. Visual inspection of interference fringes showed film growth was most rapid in the centre of the film, where the underlying carbon heating block was slightly hotter (Fig. 1). Although the carbon heating block used to heat the substrate during the deposition reaction is fairly uniform, a slight heating gradient of *ca.* 25 °C was noted, with the hottest point in the centre. This correlated with where film-growth was most rapid, indicative of a surface-reaction rate limited reaction as far as the oxide was concerned. Film thickness varied from 100 to 715 nm (Fig. 6b), with an overall median growth rate of 11.7 nm/s with a standard deviation of 4.5 nm/s at a substrate temperature of 500 °C.

Table 4
Precursor flow rates, vapour pressures, mass flows and molar ratios for the cAPCVD formation of a combinatorial anatase TiO_2 thin-film with gradating N-dopant levels and insertion type from predominantly N_s to purely N_i-doping.

Precursor	F (L min^{-1})	Vp (mm Hg)	a (mol min^{-1})	Molar ratios
$TiCl_4$	2.0	32.9	0.0037	1.0
Ethyl acetate	0.8	215	0.0129	3.5
NH_3	0.02	n/a	0.0008	0.2

The level of nitrogen incorporation varied across the film (Table 3), with little bearing on the underlying thickness. The most concentrated N-dopant levels determined by XPS (Table 3) were local to the nitrogen source gas-inlet (J3) and along Column D, which lay in line of sight of the ammonia gas flow. The lowest overall level of N-doping was observed at J33, that lay furthest from the nitrogen source-gas inlet in the lateral plane; demonstrating a mass transport limitation of the nitrogen source. This correlated directly to the type of N-doping that took place, where a lower local ammonia concentration induced interstitial doping over substitutional. The mass transport limitations of the nitrogen source in addition to the carbon block heating gradient engineered variations in nitrogen levels, type of N-insertion (N_s/N_i) and film thicknesses; desired for the combinatorial aspect of this work.

Given the approximately uniform deposition temperature of 500 °C, it was expected that only the anatase TiO_2 phase formation occurred as the thermodynamically more favourable rutile phase typically requires more elevated temperatures in CVD processes (>600 °C) [19]. Nonetheless, a variation in the crystallinity across the film was observed. Positions most local to the precursor gas-inlets (Rows 1–10) were predominantly amorphous whereas positions furthest from the inlets showed the highest degrees of film crystallinity (Fig. 3). This was attributed to two factors: (i) positions near the middle-bottom section of the film experienced a slightly greater deposition temperature due to the variation in the carbon block heating gradient and (ii) positions near the gas-inlets experienced a high pressure of precursors before equalising further into the reactor, which possibly inhibited film growth. However, a reverse effect was observed in the film's surface roughness, where smoother surfaces were formed at positions more local to the gas-

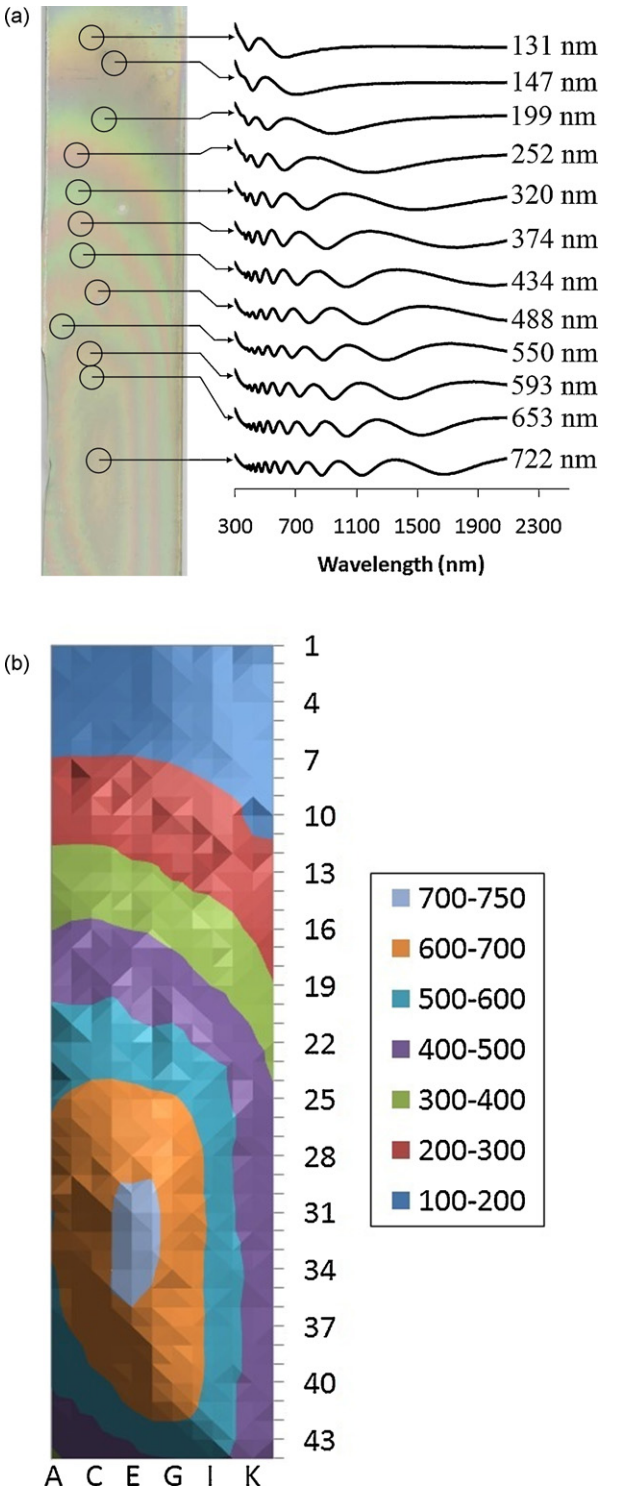

Fig. 6. (a) A map showing the precise locations where transmittance (%) spectra were recorded between interference contours. The stack graph (arbitrary units) displays the increasing wavy nature of transmittance spectra with increased thickness and quantified by the Swanepoel method. Assuming linear growth between interference contours, the thickness at each position was calculated and displayed in (b) a colour coded contour map of film thickness for all 528 grid positions on the combinatorial film.

inlets (Fig. 5). As precursors initially pass through a baffle manifold, which induces laminar flow before reactor entry, a less chaotic gas mix was experienced in the early rows. Further into the reactor, it is expected that more turbulent mixing of gas flows would have occurred, causing courser film growth.

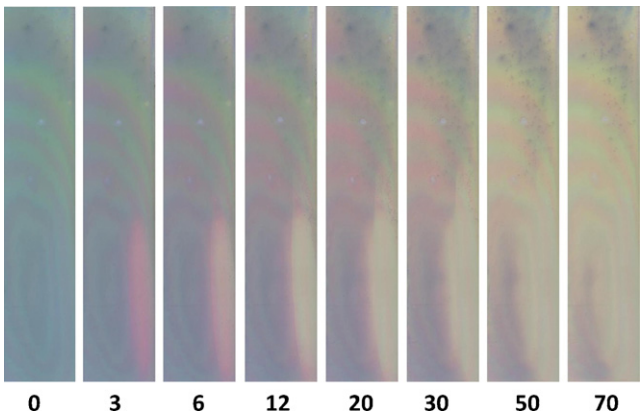

Fig. 7. Select images of the photo-reduction reaction of an even intelligent ink layer by 365 nm UVA-light (1.75 mW cm^{-2}) at 0, 3, 6, 12, 20, 30, 50 and 70 min irradiation. The greatest activity was observed in the interstitial N-doped section of the anatase TiO_2 thin-film; gradating film from predominantly N_s to purely N_i-doping synthesised by a cAPCVD technique.

3.3. Photocatalytic activity

The photocatalytic activities were assessed using an aerosol-spray area analysis method [53,54]. The pre-photocatalytically charged combinatorial thin-film was spray-coated with an even layer of intelligent ink as formulated by Mills et al. [61]. The coated film was then subjected to 365 nm UVA-irradiation (1.75 mW cm^{-2}) and the photocatalytic degradation of the dye monitored by digital photography between irradiations (Fig. 7).

The ink functions *via* a photo-reduction mechanism [63]. Upon photo-excitation of a semiconductor thin-film, electrons and holes migrate to the surface. The excess sacrificial electron donor (glycerol) within the ink reacts with surface holes, stabilising surface electrons to recombination processes. These electrons subsequently reduce the redox dye Resazurin (royal blue) to Resorufin (pink) in a two electron two proton process, which is further reduced to bleached intermediates (colourless) in additional reduction cycles.

A non-homogenous yet smooth transition from blue (Resazurin) to pink (Resorufin) to colourless (bleached intermediates) ink layers were observed in the photoreduction reaction. A representative set of select images for the photo-reduction reaction are shown in Fig. 9. The initial change from blue to pink occurred in the bottom right section of the film, where a transition to an intense pink was seen after just 3 min exposure to UVA-light. Further transitions, after subsequent re-exposures, occurred outwardly in an approximately diagonal fashion from the most active bottom-right section. After 20 min irradiation, a large area of the bottom-right section had turned colourless, indicative of a complete reduction of the dye to bleached products. After 70 min of irradiation, most of the dye within the ink-grid had been bleached. However, significant portions in the bottom-left and top-middle areas of the film were yet to turn colourless and it was clear that the underlying semiconductor at these positions were of relatively low photo-activity to 365 nm light.

Using software built in-house entitled RGB Extractor© [62] the changes in red-green-blue components of digital colour at all 528 grid-positions were assessed for each image taken. Changes in the red and green components of digital colour had similar forms to what had been previously reported in the literature; with the red component tending to rise to a maximum level and the green component first reaching a minimum and then rising to a plateau [48,53,54]. Changes in the red and green components of digital colour were directly related to the rate of conversion of Resazurin to Resorufin [53,54]. The maximisation in the red component signified

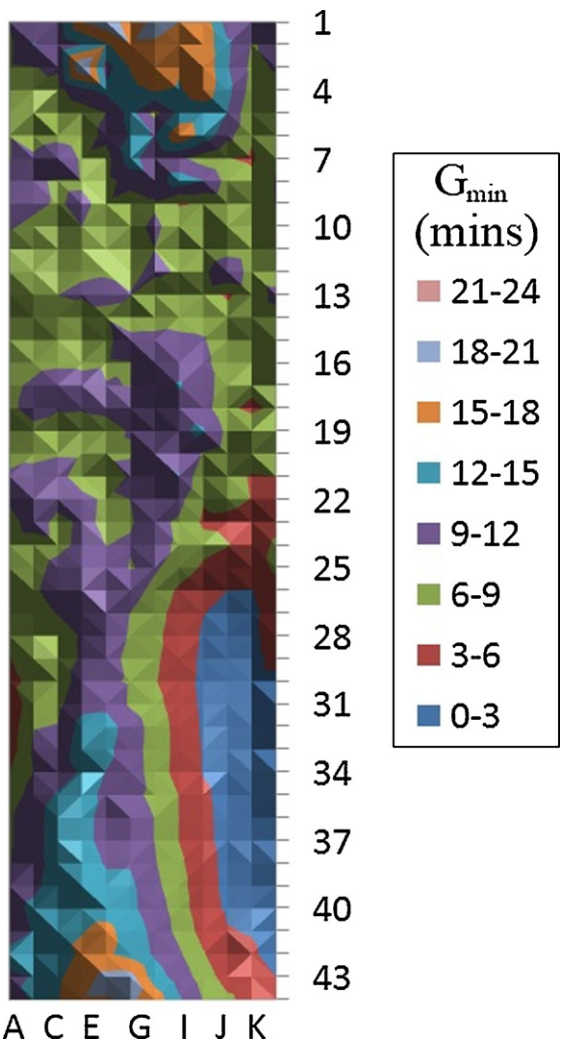

Fig. 8. 3-dimensional plot of the time taken (minutes) to reach the minimum in the green component (G_{min}) of digital colour from assessing changes in digital colour from digital images taken during the photo-reduction reaction of intelligent ink sprayed evenly onto the combinatorial film. A more rapid activity to the dye was observed in the bottom right section of the film where purely N_i-insertion was noted by XPS.

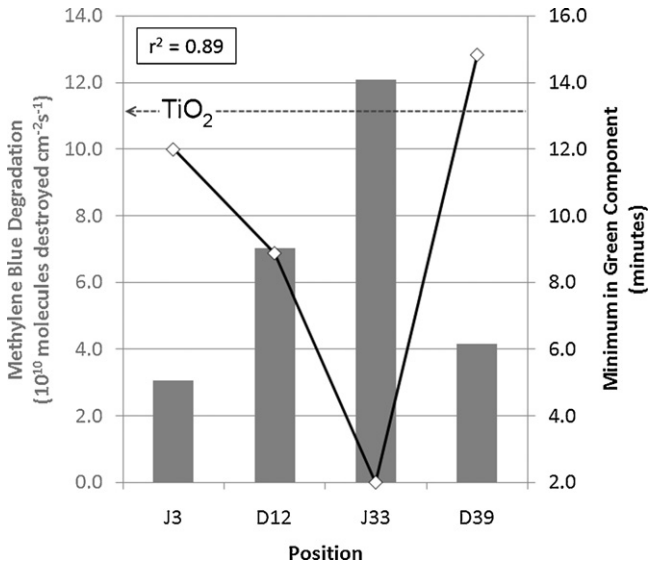

Fig. 9. A combined bar chart of photocatalytic degradation of methylene blue dye (10^{10} molecules destroyed $cm^{-2}\,s^{-1}$) to 365 nm light in solution versus a line chart of time taken to reach a minimum in the green component of digital colour (min). The degradation rate of an APCVD prepared TiO_2 standard synthesised under similar conditions to the combinatorial film is also shown by a dotted black line. An excellent correlation between the two photocatalytic testing methods is also observed ($r^2 = 0.89$).

a complete conversion of the Resazurin dye whilst the minimisation in the green component signified a maximum Resorufin intermediate formation. The rate of this photoreduction reaction is directly related to the rate of photocatalysis [61].

By modelling the red and green components to Boltzmann and bi-phasic equations respectively (supplementary information 2), the end-points for the full conversion of Resazurin (time to reach a maximum in the red component— R_{max}) and maximum in intermediate Resorufin formation (time to reach a minimum in the green component—G_{min}) could be derived. Using Origin 8.0 software [66], the data from 528 positions was rapidly modelled in a semi-automated fashion. Encouraging agreements with data to the models were observed with r^2(Boltzmann) = 0.99 ± 0.02 and r^2(Bi-phasic) = 0.96 ± 0.04 (median ± standard deviation). The distribution of G_{min} is shown in Fig. 8 (R_{max} supplied in supplementary information 3), where lower times represent quicker rates of conversion.

From the proceeding photo-reduction reaction, four distinctly different areas of varying photocatalytic activity to 365 nm light were observed: (i) rapid acting (bottom-right section), (ii) medium acting (middle section), (iii) mediocre acting (bottom-left section) and (iv) slow acting (top-middle section). Representatives of these sections (i) J33, (ii) D12, (iii) D39 and (iv) J3 were analysed by XPS (Table 3) and their photocatalytic activity to 365 nm light tested by a more traditional method; the photo-degradation of methylene blue in solution. The rates of photo-destruction for the four representative positions are shown in Fig. 9.

A complementary inverse correlation between the rate of methylene blue destruction and minimum in the green component from the intelligent ink test was observed with good agreement ($r^2 = 0.89$). The purely N_i-doped sample (J33) was the most active in both photocatalytic tests to UVA-light and fared slightly better than a pure anatase TiO_2 standard, formed by APCVD under analogous conditions to the combinatorial film; bar ammonia insertion. Although the crystallinity, surface roughness and film thickness local to position J33 were considerably higher compared with positions J3 and D12, they were practically equivalent to positions local to D39. This allowed for a fair comparison between these two grid-positions, where J33 was approximately 3 times more active than D39. The explanation for the varying photocatalytic activities seen could be explained by comparing the level of N_s-doping within the sample. An inverse correlation between N_s-doping and photocatalytic activity to methylene blue degradation was observed, with excellent agreement ($r^2 = 0.99$).

There is a wide consensus to N_s-doping of titania causing a bandgap narrowing, red-shifting the photo-excitation energy toward the visible [28–33]. DFT studies have also shown that N_i-doping of anatase causes the formation of an inter-band state approximately midway between the valence and conduction band [38–41]. Nevertheless, there is conflict as to whether N_s or N_i-doping of anatase leads to any photocatalytic enhancements under UVA-light.

It was recently shown that photocatalytically charged N_s-doped titania films display almost instantaneous electron–hole recombination in the dark, whereas photo-generated electron–holes in un-doped anatase remained stable in the dark for appreciably longer periods [67]. This indicated photo-generated electron–holes in N_s-doped anatase were more susceptible to recombination processes which could explain their lowered activity to UVA-light

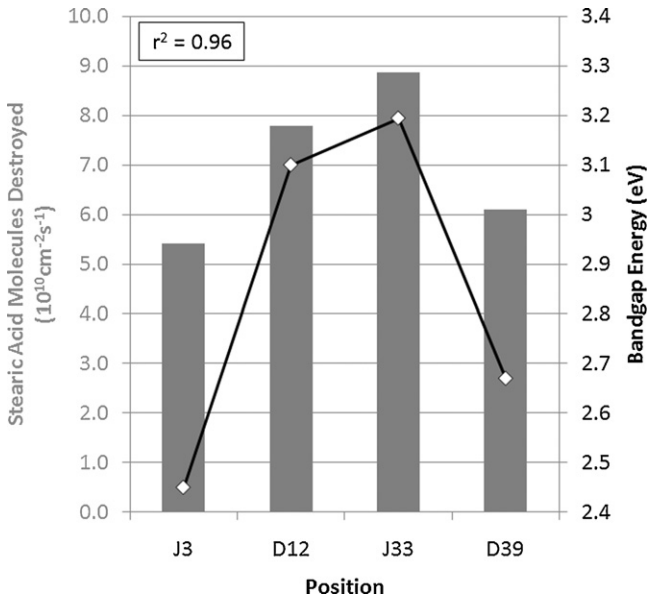

Fig. 10. A combined bar chart of photocatalytic degradation of a stearic acid overlayer (10^{10} molecules destroyed cm^{-2} s^{-1}) to a white light source versus a line chart of the calculated bandgap. The degradation rate of an APCVD prepared TiO_2 standard synthesised under similar conditions to the combinatorial film was negligible. A counter-intuitive correlation between the bandgap energy and visible light activity was observed ($r^2 = 0.96$) explained by increased recombination effects.

vide-infra. The subtle balance between red-shifted photo-excitation energies in N_s-doped anatase and the stability of photo-generated electron–holes is therefore of key importance. Although high levels of N_i-doping were observed at position J33 (4.3 at.%), a slight increase in the photocatalytic activity relative to a titania standard was observed (Fig. 9). Although the enhancement in the activity was not hugely significant, it was indicative of increased stability of photo-generated electron–holes in N_i-doped over N_s-doped anatase.

The visible light photocatalytic activities of the four representative positions were subsequently tested against a white light source equipped with a UV-filter to a stearic acid layer (Fig. 10). Over a 50 h period of testing, the most photocatalytically active position was again observed at position J33, the solely N_i-doped position. Conversely, the lowest visible light activity to stearic acid degradation was seen at position J3, the most heavily N_s-doped of the four representative positions. This was irrespective of the Tauc plot derived bandgap energy, where most dramatic red-shift occurred at position J3 (2.45 eV). Given position J3 was not as crystalline or rough as the other representative positions, it would be unfair to wholly account for these lower photocatalytic activities observed from N_s-levels. Of the four representative positions, only positions J33 and D39 were comparatively equal in all physical properties bar one; nitrogen content/type. Comparing the visible light activity of these positions reveals two key points: (i) a narrowing of the bandgap energy does not necessarily mediate more visible light activity and (ii) solely N_i-doping of anatase shows marginally better visible light photocatalytic activity than predominantly N_s-doping. Although no alteration in the valence-conduction band energy was seen at position J33 (3.19 eV), it was deduced that the inter-band state formed by N_i-doping of anatase [38–40] might not be directly observable by UV–visible spectroscopic methods. This would explain the visible light activity seen at position J33 whereas an un-doped anatase counterpart showed negligible activity.

The level of N_i-insertion observed at position J33 (4.3 at.%) was considerably higher than what was observed in previous APCVD studies of N_i-doped anatase thin-films; where levels up to only ≈0.5 at.% were achieved [34–36]. However, significant visible light enhancements were also observed at these low insertion levels.

In Fig. 10, a counter intuitive relationship between the material's bandgap narrowing and visible light activity ($r^2 = 0.96$) was observed where decreases in band energy yielded less visible light active positions. This was related entirely to the effect of N_s-doping, where increased levels yield a reduced bandgap yet possibly increased photo-generated electron–hole recombination. This was verified by the strong inverse relationship between the level of N_s-doping and visible light ($r^2 = 0.91$), where increased N_s-doping led to a worsened visible light photocatalyst.

When comparing the results from the two traditional photocatalytic testing methods used in this study; the degradation of methylene blue solution by UVA-light and the degradation of stearic acid by white light, a fundamental pattern is observed. In both cases, position J33 was most active, followed by positions D12, D39 and J3. Comparing positions of approximately equivalent crystallinity, surface roughness and thickness; pure N_i-doping of anatase (J33) formed a marginally more active visible light photocatalyst (≈30% more active; Fig. 10) and a considerably more UVA-light active photocatalyst (190% more active; Fig. 9) than a predominantly N_s-doping (D39). These combined properties seemingly make purely N_i-doped anatase films more attractive than N_s-doped films not only for indoor self-cleaning applications but also for outdoor uses that take advantage of the entire solar spectrum (UV and visible light).

4. Conclusion

Combinatorial anatase thin-films with gradating nitrogen dopant levels and insertion from predominantly substitutional doping to purely interstitial doping were synthesised by cAPCVD. A triple source of precursors was used with $TiCl_4$ as the metal source, ethyl-acetate as the oxygen source and NH_3 gas as the nitrogen source. We believe this to be the first time that such a gradient from interstitial to substitutional doping has been achieved by a CVD process. The film consisted of nitrogen dopant concentration and insertion type, crystallinity, preferred orientation growth, surface roughness and thickness gradients; adding to the combinatorial nature of the film wholly desired for the full investigation of an array of physical effects on the film's functional properties.

Mapping of the combinatorial film's photocatalytic activity to UVA and white light sources, in conjunction with physical characterisation methods, allowed for the systematic investigation on the effect of nitrogen doping. It was found that the most photo-active section of the film to UVA-light contained solely interstitial nitrogen doping and was moderately more active than an un-doped titania standard. Photocatalytic activity decreases were also proportional to the level of substitutional doping in UVA-light reactions. All films showed visible light activity regardless of the type of nitrogen dopant; however the most active film contained solely interstitial nitrogen doping and was 30% more active than a comparable predominantly substitutional doped counterpart. The photocatalytic activity differences in interstitial and substitutional nitrogen doping were related to the greater stability of photo-generated electron–holes in interstitially doped anatase and the greater propensity for recombination processes to occur in substitutional nitrogen doped materials.

Films synthesized by the cAPCVD route analysed in conjunction with mapping analysis tools provide a shortcut to identifying numerous phases and compositions and their functional property relationships on a single film, offering a rapid method for analysis of phase-space.

Acknowledgements

IPP wishes to thank the Royal Society and Wolfsen Trust for a merit award and express gratitude to Prof. Andrew Mills (Strathclyde) for the intelligent ink used in photocatalysis studies and Cardiff University for allowing the use of their XPS instrument. EPSRC are thanked for funding.

Appendix A. Supplementary data

Supplementary data associated with this article can be found, in the online version, at doi:10.1016/j.jphotochem.2010.06.034.

References

[1] A. Mills, S. LeHunte, J. Photochem. Photobiol. A 108 (1997) 1.
[2] A. Fujishima, X. Zhang, D.A. Tryk, Surf. Sci. Rep. 63 (2008) 515.
[3] V. Keller, N. Keller, M.J. Ledoux, Chem. Commun. 1 (2005) 2918.
[4] T. Nonami, H. Hase, K. Funakoshi, Catal. Today 96 (2004) 113.
[5] W. Jacoby, P.C. Maness, E.J. Wolfrum, Environ. Sci. Technol. 32 (1998) 2650.
[6] T. Matsunaga, T. Nakajima, Appl. Environ. Microb. 50 (1985) 238.
[7] R.J. Watts, S.H. Kong, M.P. Orr, Water. Res. 95 (1995) 95.
[8] T. Matsunaga, R. Tomoda, T. Nakajima, Appl. Environ. Microb. 54 (1988) 1330.
[9] J.C. Ireland, P. Klostermann, E.W. Rice, Appl. Environ. Microb. 59 (1993) 1668.
[10] Z. Huang, P.C. Maness, S. Smolinski, J. Photochem. Photobiol. A 28 (1999) 1.
[11] K.P. Kuhn, I.F. Chaberny, K. Massholder, Chemosphere 53 (2003) 71.
[12] G.F. Fu, P.S. Vary, C.T. Lin, J Phys. Chem. B 109 (2005) 8889.
[13] J.C. Yu, W.K. Ho, J. Lin, Environ. Sci. Technol. 37 (2003) 2296.
[14] I.P. Parkin, K. Page, R.G. Palgrave, J. Mater. Chem. 17 (2007) 95.
[15] Pilkington NSG Group Flat Glass Business http://www.pilkingtonselfcleaningglass.co.uk/, last accessed 17th April 2010.
[16] TOTO Hydrotect http://www.toto.co.jp/en/abstract/today/pdf/04_0130today.pdf, http://eu.toto.com/site/TOTO/Templates/Hydrotect.aspx?pageid=131&cc=GB, last accessed 17th April 2010.
[17] I.P. Parkin, R.G. Palgrave, J. Mater. Chem. 15 (2005) 1689.
[18] S.A. O'Neill, I.P. Parkin, R.J.H. Clark, A. Mills, N. Elliott, J. Mater. Chem. 13 (2003) 56.
[19] G. Hyett, M. Green, I.P. Parkin, J. Am. Chem. Soc. 128 (2006) 12147.
[20] S.D. Sharma, D. Singh, K.K. Saini, Appl. Catal. 314 (2006) 40.
[21] E. Celik, Z. Gokcen, N.F.A. Azem, Mater. Sci. Eng. B Solid 132 (2006) 258.
[22] R.S. Sonawane, M.K. Dongare, J. Mol. Catal. A: Chem. 243 (2006) 68.
[23] I.P. Parkin, A. Rampaul, S.A. O'Neil, Polyhedron 22 (2003) 35.
[24] M. Wong, S. Hsu, K.K. Rao, C.P. Kumar, J. Mol. Catal. A: Chem. 279 (2008) 20.
[25] T. Lopez-Luke, A. Wolcott, L.P. Xu, S.W. Chen, Z.H. Wcn, J.H. Li, E. De La Rosa, J.Z. Zhang, J. Phys. Chem. C 112 (2008) 1282.
[26] J.K. Zhang, W. Xu, X.J. Li, S.J. Zheng, G. Xu, Cent. Eur. J. Chema. 4 (2006) 234.
[27] A. Kafizas, S. Kellici, J.A. Darr, I.P. Parkin, J. Photochem. Photobiol. A 204 (2009) 183.
[28] R. Asahi, T. Morikawa, T. Ohwaki, K. Aoki, Y. Taga, Science 293 (2001) 269.
[29] H. Irie, Y. Watanabe, K. Hashimoto, J. Phys. Chem. B 107 (2003) 5483.
[30] K. Pomoni, A. Vomvas, C. Trapalis, J. Non-Cryst. Solids 354 (2008) 4448.
[31] S. Mahalingam, M.J. Edirisinghe, J. Phys. D: Appl. Phys. 41 (2008) 215406.
[32] S. Livraghi, K. Elghniji, A.M. Czoska, M.C. Paganini, E. Giamello, M. Ksibi, J. Photochem. Photobiol. A 205 (2009) 93.
[33] S. Livraghi, M.R. Chierotti, E. Giamello, G. Magnacca, M.C. Paganini, G. Cappelletti, C.L. Bianchi, J. Phys. Chem. C 112 (2008) 17244.
[34] C.W. Dunnill, Z.A. Aiken, J. Pratten, M. Wilson, D.J. Morgan, I.P. Parkin, Photochem. Photobiol. A 207 (2009) 244.
[35] C.W. Dunnill, Z.A. Aiken, A. Kafizas, J. Pratten, M. Wilson, D.J. Morgan, I.P. Parkin, J. Mater. Chem. 19 (2009) 8747.
[36] C.W. Dunnill, I.P. Parkin, Chem. Vapor Depos. 15 (2009) 171.
[37] L. Zhao, Q. Jiang, J. Lian, Appl. Surf. Sci. 254 (2008) 4620.
[38] C. Di Valentin, E. Finazzi, G. Pacchioni, A. Selloni, S. Livraghi, M.C. Paganini, E. Giamello, Chem. Phys. 339 (2007) 44.
[39] C.D. Valentin, G. Pacchioni, A. Selloni, S. Livraghi, E. Giamello, J. Phys. Chem. B 109 (2005) 11414.
[40] Z. Zhao, Q. Liu, J. Phys. D: Appl. Phys. 41 (2008) 1.
[41] F. Peng, L. Cai, H. Yu, H. Wang, J. Solid State Chem. 181 (2008) 130.
[42] U. Qureshi, C. Blackman, G. Hyett, I.P. Parkin, Eur. J. Inorg. Chem. 10 (2007) 1415.
[43] S. O'Neill, I.P. Parkin, R.J.H. Clark, A. Mills, N. Elliott, Chem. Vapor Depos. 10 (2004) 136.
[44] A. Mills, G. Hill, S. Bhopal, I.P. Parkin, S. O'Neill, J. Photochem. Photobiol. A 160 (2003) 185.
[45] G. Yu, X. Zhang, G. Han, Mater. Sci. Eng. B: Solid 135 (2006) 83.
[46] S.A. O'Neill, R.J.H. Clark, I.P. Parkin, Chem. Mater. 15 (2003) 46.
[47] A. Kafizas, G. Hyett, I.P. Parkin, J. Mater. Chem. 19 (2009) 1399.
[48] A. Kafizas, I.P. Parkin, J. Mater. Chem. 20 (2010) 2157.
[49] A. Kafizas, C.W. Dunnill, G. Hyett, I.P. Parkin, ECS Trans. 25 (2009) 1239.
[50] G. Hyett, M. Green, I.P. Parkin, J. Am. Chem. Soc. 129 (2007) 15541.
[51] G. Hyett, M.A. Green, I.P. Parkin, Chem. Vapor Depos. 14 (2008) 309.
[52] G. Hyett, I.P. Parkin, Surf. Coat Technol. 201 (2007) 8966.
[53] A. Kafizas, D. Adriaens, A. Mills, I.P. Parkin, Phys. Chem. Chem. Phys. 11 (2009) 8367.
[54] A. Kafizas, A. Mills, I.P. Parkin, Anal. Chim. Acta 663 (2010) 69.
[55] H.M. Yates, M.G. Nolan, D.W. Sheel, M.E. Pemple, J. Photochem. Photobiol. A 179 (2006) 213.
[56] F.D. Duminica, F. Maury, R. Hausbrand, Surf. Coat Technol. 201 (2007) 9349.
[57] R. Swanepoel, J. Phys. E: Sci. Instrum. 16 (1983) 1214.
[58] B. von Blanckenhagen, D. Tonova, J. Ullmann, Appl. Opt. 41 (2002) 3137.
[59] CASA Software http://www.casaxps.com/, last accessed 18th April 2010.
[60] Salle, Sauerlander, Practical Surface Analysis, vol. 1, second edition, John Wiley and Sons, Chichester, 1993, p. 635.
[61] A. Mills, J. Wang, M. McGrady, J. Phys. Chem. B 110 (2006) 18324; Mills, M. McFarlane, Catal. Today 129 (2007) 28.
[62] RGB Extractor, http://www.chem.ucl.ac.uk/people/ipparkin/documents/RGB_Extractor_2_1.zip.
[63] A. Mills, J. Wang, S. Lee, M. Simonsen, Chem. Commun. (2005) 2721.
[64] A.L. Patterson, Phys. Rev. 56 (1939) 978.
[65] R.J. Betsch, J. Cryst. Growth 77 (1986) 210.
[66] Origin 8, http://www.originlab.com/ last accessed 19th April 2010.
[67] R. Beranek, H. Kisch, Electrochem. Commun. 9 (2007) 761.